

Investigations of the formation of zeolite ZSM-39 (MTN)

Zheng Sonia Lin, Donghan Chen, Heng-Yong Nie, Y.T. Angel Wong, and Yining Huang

Abstract: Crystallization of zeolite ZSM-39 (MTN), a clathrate and silicate analogue of the 17 Å cubic gas hydrate, was examined in a solvent system involving a tetramethylammonium chloride – 1,6-hexanediol deep eutectic mixture and significant amount of water. The crystallization process was followed by powder X-ray diffraction (PXRD), and solid-state nuclear magnetic resonance (SSNMR) techniques involving several nuclei such as ^{19}F , ^{29}Si , and ^{13}C . The results indicate that the crystallization starts from the arrangement of amorphous Si–O–Si species around the tetramethylammonium ions and subsequent formation of the cages in the precursors similar to $[\text{5}^{12}\text{6}^4]$ cages in the MTN topology. The larger $[\text{5}^{12}\text{6}^4]$ cages are then connected via the smaller $[\text{5}^{12}]$ cages containing the fluoride ions to form the final MTN structure. Scanning electron microscopy (SEM) and atomic force microscopy (AFM) analyses show that the crystal growth rates along $\langle 100 \rangle$ and $\langle 111 \rangle$ directions are roughly the same, suggesting that the (100) and (111) planes have similar stability under the crystallization conditions used. AFM study also shows that the freshly born nuclei on the (100) face are of a height of 2 nm, suggesting a layer by layer growth of the polyhedral crystal.

Key words: ZSM-39, zeolites, deep eutectic mixture, crystallization.

Résumé : Nous avons étudié la cristallisation de la zéolithe ZSM-39 (MTN), un clathrate et analogue silicaté de l'hydrate de gaz à structure cubique de 17 Å, dans un système de solvants composé d'un mélange eutectique profond de chlorure de tétraméthylammonium – 1,6-hexanediol et d'une importante quantité d'eau. Nous avons suivi le processus de cristallisation par diffraction des rayons X sur poudre (DRXP) et par résonance magnétique nucléaire à l'état solide (RMNes) de plusieurs noyaux, tels que ^{19}F , ^{29}Si et ^{13}C . Les résultats indiquent que la cristallisation commence par l'organisation d'espèces amorphes de Si–O–Si autour des ions tétraméthylammonium et qu'elle se poursuit par la formation des cages dans les précurseurs de manière analogue à celle des cages $[\text{5}^{12}\text{6}^4]$ de topologie MTN. Les grandes cages $[\text{5}^{12}\text{6}^4]$ se fixent ensuite à de plus petites cages $[\text{5}^{12}]$ contenant l'ion fluor pour former la structure MTN finale. Des analyses par microscopie électronique à balayage (MEB) et microscopie à force atomique (AFM) montrent que les vitesses de croissance du cristal sont sensiblement les mêmes le long des axes $\langle 100 \rangle$ et $\langle 111 \rangle$, ce qui permet de penser que la stabilité est semblable dans les plans (100) et (111) dans les conditions de cristallisation employées. L'analyse par AFM montre également que les noyaux nouvellement formés sur la face (100) sont d'une hauteur de 2 nm, ce qui laisse supposer que le cristal polyédrique croît couche par couche. [Traduit par la Rédaction]

Mots-clés : ZSM-39, zéolites, mélange eutectique profond, cristallisation.

Introduction

Zeolites are crystalline microporous silicates or aluminosilicates. They are important in various industrial processes.¹ The formation of zeolites often requires the presence of an organic structure-directing agent (SDA), which tends to be occluded in the pores of the final product.² Studies of the location of these SDAs in the framework allow us to have a better understanding of the crystallization process of these microporous materials.

Zeolite ZSM-39 (which has MTN topology) is a clathrate and the silicate analogue of the 17 Å cubic gas hydrate.³ It is usually made under hydrothermal and non-aqueous conditions.^{4–7} One of the most commonly used SDA in the synthesis of ZSM-39 is tetramethylammonium ion (TMA^+). The MTN framework consists of two different cage systems, namely $[\text{5}^{12}]$ and $[\text{5}^{12}\text{6}^4]$ (Fig. 1).^{3,6} Due to the small diameter of the $[\text{5}^{12}\text{6}^4]$ cages (7.44 Å) and the size restriction on the molecules that can diffuse along the very narrow channels (2.61 Å), ZSM-39 has very limited sorption ability.⁶ It is well known that the SDA molecules are often occluded inside the zeolite frameworks when crystallization is complete.⁸ Due to the small

cages present in ZSM-39's clathrate type of structure, any molecules or ions that have entered the system during the crystallization cannot escape. Therefore, despite of its limited sorption abilities, ZSM-39 is an excellent candidate for studying guest–host interactions under different synthetic conditions. Studying these interactions involving SDA and monitoring the changes in the chemical environment around SDA during crystallization will shed light on the mechanisms of the framework formation. Previous work found that under hydrothermal conditions, the addition of DL-histidine to the reaction gel containing tetramethylammonium hydroxide (TMAOH) as the SDA for synthesis of zeolite dodecasil-3C (which also has MTN structure) can promote crystallization over nucleation, which results in larger crystal sizes.⁹ Another study was also performed on the formation mechanism of ZSM-39 using tetramethylethylenediamine (TMEDA) as the organic SDA under hydrothermal conditions.¹⁰ The study found that the silicate species in the gel first aggregates around the TMEDA. Then, condensation of silica occurs to form the zeolite framework. The TMEDA is eventually incorporated into the ZSM-39 structure.

Received 10 March 2019. Accepted 16 August 2019.

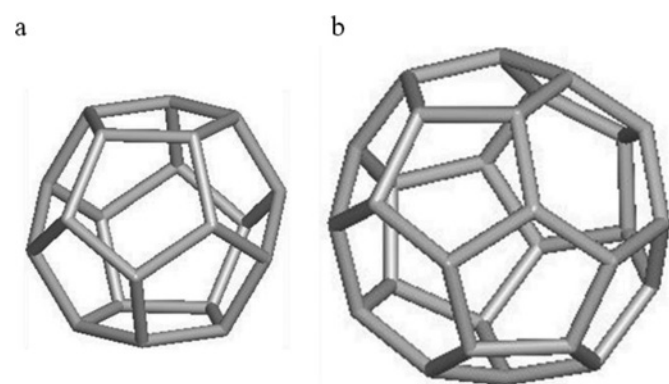
Z.S. Lin, D. Chen, Y.T.A. Wong, and Y. Huang. Department of Chemistry, The University of Western Ontario, London, ON N6A 5B7, Canada. H.-Y. Nie. Surface Science Western, The University of Western Ontario, London, ON N6G 0J3, Canada.

Corresponding author: Yining Huang (email: yhuang@uwo.ca).

Yining Huang currently serves as the Editor-in-Chief, peer review and editorial decisions regarding this manuscript were handled by David Bryce and Frank Schaper.

Copyright remains with the author(s) or their institution(s). Permission for reuse (free in most cases) can be obtained from [RightsLink](https://www.nrcresearchpress.com/cjc).

Fig. 1. Two types of cages that MTN structure is built upon: (a) $[5^{12}]$ and (b) $[5^{12}6^4]$.



High silica zeolites are generally synthesized hydrothermally at temperatures between 150 and 200 °C by mixing silica, water, base, and SDA. Due to the large amount of water present, this reaction system generates autogenous pressure. Over the past few decades, there have been attempts to synthesize zeolites in non-aqueous systems containing organic solvents or in mixed solvents.^{11–18} More recently, a newer synthetic strategy using ionic liquid (IL) to prepare framework structures has been developed. One class of ILs is deep eutectic solvents (DESs). A DES is a mixture containing two compounds with its melting point lower than individual components. Dong's group first demonstrated that $\text{AlPO}_4\text{-n}$ based molecular sieves can be prepared in a DES containing an organic salt acting as SDA and pentaerythritol, which was used as part of the DES to bring down the melting point of the mixture.¹⁹

Examples of synthesis of silicate- or aluminosilicate-based molecular sieves in the ILs containing imidazolium ion or the DES containing tetraalkylammonium SDA are relatively rare.^{20–27} The reason for this is due to the low solubility of silica in ILs and (or) DESs. Although there have been reports on the crystallization of zeolites under hydrothermal conditions, no extensive mechanistic studies have been performed on the formation of zeolites in a solvent system containing DES. Such investigations are necessary for understanding the high-silica zeolite production in ILs, the preparation of other framework types, and the development of new structures. The present work focuses on an investigation of crystallization of ZSM-39 in a solvent system with a eutectic mixture of tetramethylammonium chloride (TMACl) and 1,6-hexanediol, fluoride ions as mineralizing agent, and water. Herein, we present the findings of this study by powder X-ray diffraction (PXRD), multi-nuclear (^{29}Si , ^{13}C , and ^{19}F) magnetic resonance (NMR) spectroscopy, scanning electron microscopy (SEM), and atomic force microscopy (AFM).

It is well known in the literature that when synthesizing high silica zeolites using ionothermal methods or in deep eutectic solvents, an appreciable amount of water was always added to the reaction mixture, as the presence of water is essential for the reactions to take place. Water plays crucial roles in the dissolution of reactant species and the condensation steps of the framework formation.^{20–29} The role of water in and the effect of water content on zeolite synthesis involving IL and DES have also been examined.^{30–32} The work by Yasaka et al. showed that water is significantly deactivated in ILs containing as much as 7 mol/L water.³¹ Ma and co-worker demonstrated that the presence of water is necessary for the ionothermal synthesis of molecular sieves and addition of reagent quantities of water can enhance the crystallization kinetics.³² In the present work, a significant amount of water comes from chemical reagents exclusively.

Experimental

Sample preparation

Ammonium fluoride (NH_4F , $\geq 98\%$, Alfa Aesar), 1,6-hexanediol (97%, Sigma-Aldrich), and TMACl (97%, Sigma-Aldrich) were mixed quantitatively and ground using a mortar and pestle. The ground solid mixture was then transferred to a 40 mL Teflon container. To this mixture, a source of colloidal silica (Ludox HS-40, Sigma-Aldrich) was added. Ludox HS-40 contains 40% SiO_2 and 60% water. The components were hand-mixed using a spatula until a sticky white paste formed inside the Teflon cup. The mole ratios of the reagents are as follows: 1.0 SiO_2 : 0.9 TMACl: 0.9 1,6-hexanediol: 1.0 NH_4F : 5.0 H_2O .

Several Teflon containers charged with the same starting materials were placed inside stainless steel autoclaves. The autoclaves were then heated in an oven at 140 °C. To obtain the intermediates, autoclaves were taken out of the oven after different time periods and immediately quenched in cold water to stop the reactions. The solid sample was then washed in an excess of solvent mixture containing 1:1 volume ratio of water and ethanol.

Sample characterization

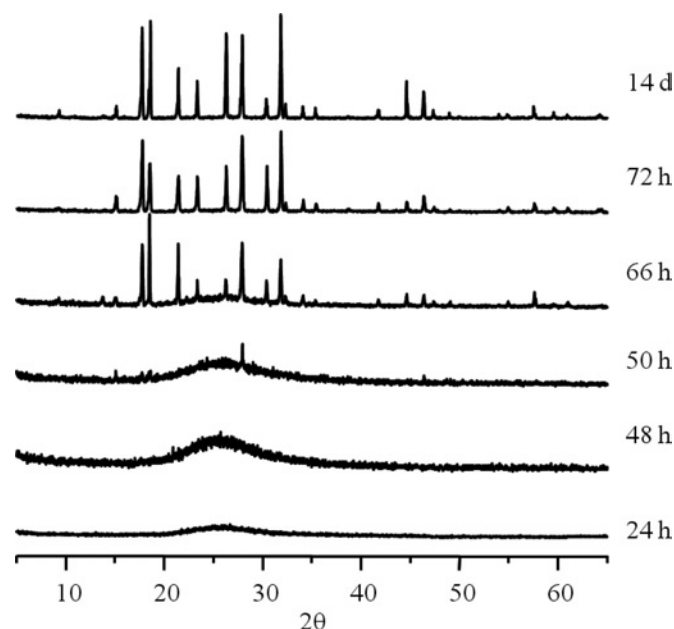
PXRD patterns of intermediates were collected on a Rigaku powder diffractometer with $\text{Co-K}\alpha$ radiation ($\lambda = 1.79 \text{ \AA}$) for 2θ values in the range of 5°–65°.

Magic-angle spinning (MAS) NMR technique was used to characterize the chemical environments of the nuclei of interest in the samples. The measurements were done on an Infinity Plus 400 spectrometer with a wide-bore magnet operating at a field strength of 9.4 T. The Larmor frequencies of ^{29}Si , ^{13}C and ^{19}F are 79.4, 100.5, and 375.9 MHz, respectively. The cross polarization (CP) experiments were set up, according to the Hartmann–Hahn conditions, on tetrakis(trimethylsilyl)-silane (TMSS) and adamantane for $^1\text{H} \rightarrow ^{29}\text{Si}$ and $^1\text{H} \rightarrow ^{13}\text{C}$ CP, respectively. ^{29}Si NMR experiments under MAS condition were performed using direct excitation and CP. Both experiments were performed using a 9.5 mm HXY probe at a spinning rate of 3.5 kHz. The ^{29}Si chemical shifts were referenced to tetramethylsilane (TMS) using the $-\text{SiMe}_3$ signal in TMSS as a secondary standard, which has an isotropic chemical shift (δ_{iso}) of -9.8 ppm with respect to TMS. For the direct-excitation experiments, a 30° pulse with a pulse delay of 30 s was used. For the $^1\text{H} \rightarrow ^{29}\text{Si}$ CP MAS experiments, a ^1H 90° pulse length of 9.5 μs and a contact time of 0.5 and 5.0 ms were used, depending on the experimental conditions. The pulse delay was 10 s. The $^1\text{H} \rightarrow ^{13}\text{C}$ CP MAS spectra of the samples were collected using a 4.0 mm MAS HXY probe; the spinning rate was 10.0 kHz. ^{13}C chemical shifts were referenced to TMS ($\delta_{\text{iso}} = 0$ ppm) by using adamantane as the external standard, which has signals at 28.8 and 38.2 ppm. The ^1H 90° pulse length was 4.5 μs . The contact time used was 3.0 ms, and the pulse delay was 10.0 s. α, α, α -Trifluorotoluene was used as an external standard ($\delta_{\text{iso}} = -63.7$ ppm with respect to CFCl_3) to reference the ^{19}F chemical shifts. For the ^{19}F MAS experiments, a 30° pulse with a pulse delay of 10 s was used. The ^{19}F MAS NMR spectra were collected by spinning the samples at 12 kHz. The isotropic peaks of these ^{19}F spectra were determined by using a different spinning rate at 10 kHz.

SEM images of the samples were collected on a LEO (Zeiss) 1530 field emission scanning electron microscope. A 3 nm conductive layer of amorphous osmium was coated onto the samples using an Osmium Plasma Coater.

AFM was performed using a Park Systems XE-100. Cantilever with nominal spring constant of 40 N/m, resonant frequency of 300 kHz, and tip radius of 10 nm (NSC15, Mikro Masch) were used under the dynamic force mode. In this mode, the cantilever is vibrated at around the resonant frequency and its amplitude reduces when the tip is in proximity with the sample surface caused by the tip – sample interaction. Reduced amplitude is set as the

Fig. 2. PXRD patterns of the samples obtained by quenching the reactions at different time intervals.



feedback parameter (set point) so that the AFM system scans the surface contour of the sample with minimized error signals (the difference between the set point and the amplitude measured) by adjusting the distance between the tip and the sample surface. Mapping of this distance constructs a topographic image for the surface morphology. On the other hand, mapping the error signal results in an image removing the height contribution and stressing only the shape of surface features. When the height range is large, surface features with small height differences are obscured. In this case, it is advantageous to use the error signal image to show the shapes of surface features, while using the topographic image to estimate the height distribution. For clarity purposes, we present AFM error signal images, rather than AFM topographic images, for the zeolite-39 crystals. The scan rate for obtaining images in an area of $45 \mu\text{m} \times 45 \mu\text{m}$ is 0.5 Hz and for images in an area of $10 \mu\text{m} \times 10 \mu\text{m}$ is 1 Hz. The experiment was conducted in air with a relative humidity of $\sim 40\%$.

Results and discussion

The crystallization process of siliceous ZSM-39 at 140°C without seeding was studied by obtaining intermediates at different reaction time intervals from 24 h to 14 days throughout the course of the reaction. The autoclaves were quenched in cold water once they were taken out the oven. PXRD patterns, ^{13}C CP MAS, ^{19}F MAS, and ^{29}Si MAS NMR spectra were collected for the samples quenched at the following time intervals: 24 h, 48 h, 50 h, 66 h, 72 h, and 14 days. $^1\text{H} \rightarrow ^{29}\text{Si}$ CP MAS NMR spectra and SEM images were obtained for selected samples. The AFM studies were performed on the 14 day sample.

At the beginning of the crystallization (heating for 24 h), the PXRD pattern indicates the sample is completely amorphous at this stage (Fig. 2). The corresponding ^{29}Si MAS NMR spectrum (Fig. 3a) indicates that the solid component of the reaction mixture contains Q^4 (Si bounded to four other neighboring Si atoms via oxygen) and Q^3 (silicon atoms bounded to three other neighboring Si atoms via oxygen and one neighboring $-\text{OH}$ group) silicon species. The chemical shift of the Q^3 silicon atoms is around -100.7 ppm, whereas the Q^4 Si sites has a chemical shift of around -111.7 ppm.³³ The $^1\text{H} \rightarrow ^{29}\text{Si}$ CP MAS NMR spectrum of 24 h sample shows the enhancement of the Q^3 peak (Fig. 3b) as the Q^3 signal is

more intense than the Q^4 signal in the CP MAS NMR spectrum. This is because CP relies on the proximity between Si atoms and protons. At the early stages of the reactions, there is unreacted amorphous silica with silanol groups on the surfaces. In unreacted silica, Q^4 is $\text{Si}(\text{OSi})_4$ and Q^3 is $\text{Si}(\text{OSi})_3(\text{OH})$. Due to the proximity between the Si and the hydrogen of the $-\text{OH}$ group, the Q^3 signal is significantly enhanced by CP. In the ^{13}C CP MAS NMR spectrum (Fig. 4), the peak at 56.2 ppm is assigned to the $-\text{CH}_3$ carbon in the TMA^+ ion. This ^{13}C signal indicates the presence of TMA^+ ions in the solid gel even before crystallization has started. The charge balancing anions in the gel is likely SiF_6^- , because a signal at -123.5 ppm is seen in the ^{19}F MAS NMR spectrum (Fig. 5). SiF_6^- has been observed as a major fluorine containing species in the gel phase in zeolite synthesis.³⁴

The PXRD pattern shows that the solid sample of reaction mixture remains amorphous after 48 h of heating (Fig. 2). There is not much change observed in the ^{13}C and direct-excitation ^{29}Si MAS NMR spectra (Figs. 3a and 4). The $^1\text{H} \rightarrow ^{29}\text{Si}$ CP MAS NMR spectrum also shows Q^3 enhancement (Fig. 3b). However, the intensity of the Q^4 peak is also enhanced with respect to the Q^3 species in the CP spectrum, compared with the 24 h sample. It appears that between 24 and 48 h, the silica in the starting material was dissolved and re-condensed to form the silicate precursors for MTN formation. The SEM image (Fig. 6i, a) shows that the majority of the sample is composed of amorphous material. However, at a higher magnification (Fig. 6i, b), the amorphous particles wrap around a chunk of solid that looks crystalline. Observing this species may indicate the beginning of the crystallization. After 50 h of reaction, the emergence of several sharp peaks belonging to ZSM-39 in the PXRD pattern marks the onset of crystallization (Fig. 2). However, no changes in chemical shifts were observed in the ^{13}C CP MAS and direct-excitation ^{29}Si MAS NMR spectra at this point (Figs. 3a and 4). The direct-excitation ^{29}Si MAS NMR spectrum consists of a rather broad and featureless Q^4 peak having a chemical shift of -111.7 ppm and a broad Q^3 peak, which is consistent with the PXRD pattern that vast majority of the solid materials are still amorphous. Nevertheless, in the $^1\text{H} \rightarrow ^{29}\text{Si}$ CP MAS NMR spectrum (Fig. 3b) collected using a 0.5 ms contact time, there is a new shoulder peak at -117.4 ppm. The intensity of this peak is markedly enhanced by using a longer contact time (10 ms), as seen in Fig. 7, and the chemical shift of this new peak coincides with the chemical shift of T_3 site (the third tetrahedral Si site) in the MTN structure.³⁵ The longer contact time discriminates against the gel phase due to the fact that the proton spin-lattice relaxation time in the rotating frame of reference ($T_{1\rho}^{\text{H}}$) in the gel phase is usually much shorter than that in the crystalline zeolites. Therefore, the $^1\text{H} \rightarrow ^{29}\text{Si}$ CP signals from the more crystalline materials can be selected. Furthermore, it is interesting to note that the intensity of the Q^4 peak is much higher in the $^1\text{H} \rightarrow ^{29}\text{Si}$ CP MAS NMR spectrum with a contact time of 10 ms. This means that there are more $\text{Si}(\text{OSi})_4$ species being organized to form precursor for MTN. For these Q^4 species, the proton source for polarization transfer is likely the hydrogen atoms in the TMA^+ ions.

The ^{13}C CP MAS NMR spectrum (Fig. 4) shows only one signal at 56.2 ppm due to the $-\text{CH}_3$ carbon. The lack of change in chemical shift in the ^{13}C spectrum indicates that the most of TMA^+ ions remained occluded inside the amorphous silica gel. As shown by SEM, the majority of the sample is still quite amorphous; however, the solid particles now seem to have more defined faces, which take the shape of a triangle (Figs. 6i, c and d). However, at this stage, we are unable to tell which face of the crystal they belong to. The structure of the MTN framework in Fig. 7 shows that the T_3 silicon atoms are located in the six-membered ring window of the $[\text{Si}^{12}\text{O}_4]$ cage. It is in this cage that the SDA resides.³⁶ Thus, the appearance of the -117.4 ppm ^{29}Si signal in both the direct-excitation MAS and CP MAS NMR spectra of the 50 h sample indicates that the T_3 sites start being formed first. It appears that some silica species aggregating around the TMA^+ begin to trans-

Fig. 3. (a) Direct-excitation ^{29}Si MAS NMR spectra of the samples obtained by quenching the reactions at different time intervals. (b) $^1\text{H} \rightarrow ^{29}\text{Si}$ CP MAS NMR spectra of samples obtained by quenching reactions at early stages of crystallization (24–50 h). A contact time of 0.5 ms was used to acquire the spectra.

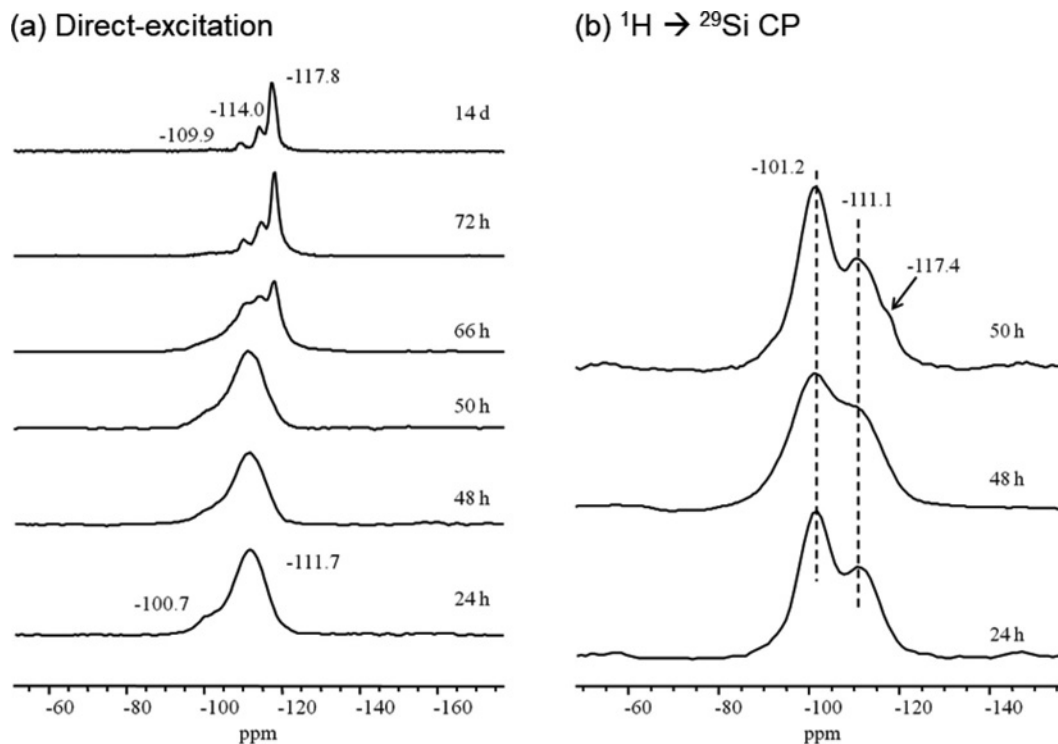
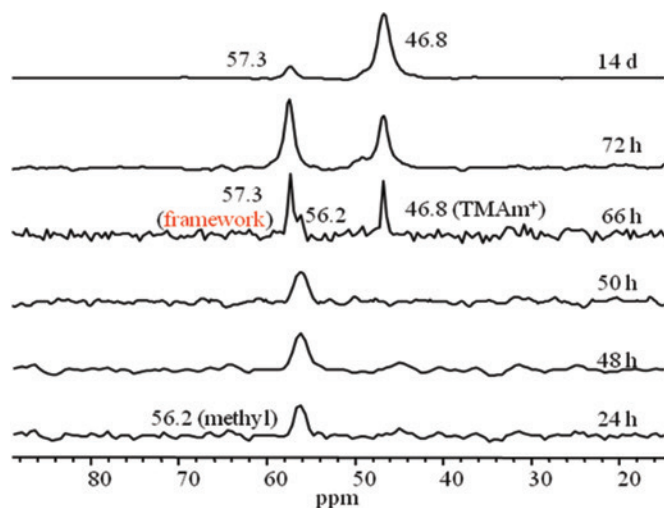


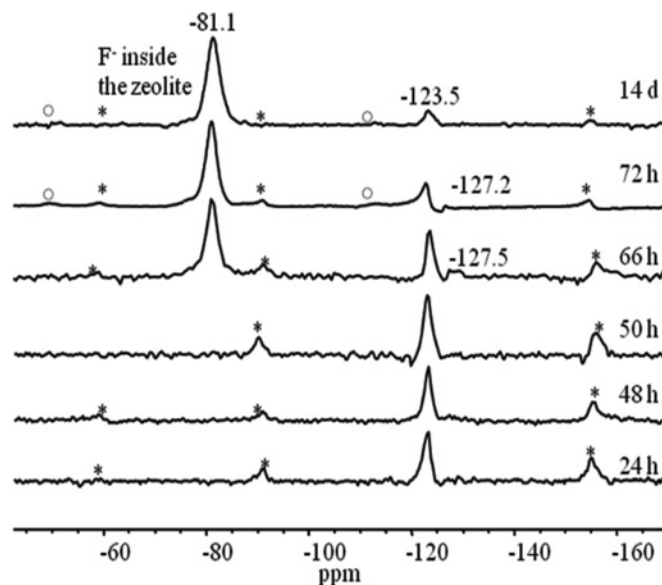
Fig. 4. $^1\text{H} \rightarrow ^{13}\text{C}$ CP MAS NMR spectra of samples obtained from reactions quenched at different time intervals. TMAm^+ = trimethylammonium ion. [Colour online.]



form to the T_3 sites, which is part of the $[\text{Si}^{12}\text{O}_4]$ cage. However, there is no change in the ^{19}F NMR spectrum at this point (Fig. 5), meaning that the F^- anions have not been occluded into the zeolite framework. This suggests that although the $[\text{Si}^{12}\text{O}_4]$ cage is forming, the smaller $[\text{Si}^{12}]$ cage (where fluoride ion is trapped) has not formed yet.

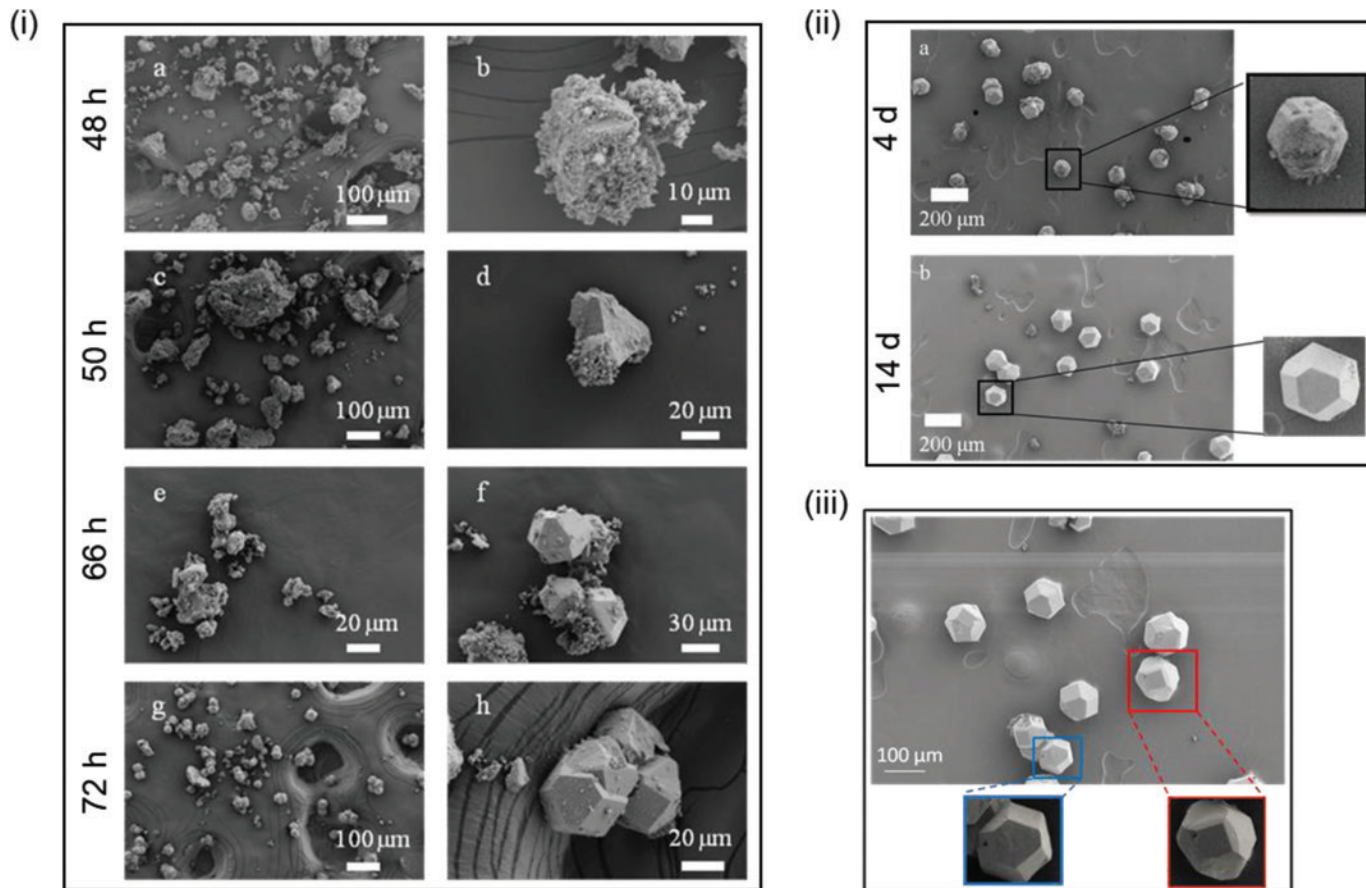
ZSM-39 crystals form very quickly after the onset of crystallization. After 66 h of heating, the reaction mixtures now contain mainly crystallized product and only a small amount of amorphous materials as marked by the broad bump at around 20° – 30° of 2θ in the PXRD pattern (Fig. 2). SEM images reveal the presence of both amorphous species and intergrown crystals of ZSM-39

Fig. 5. ^{19}F MAS NMR spectra of samples obtained from the reactions quenched at different time intervals. A spinning speed of 12 kHz was used. The spinning sidebands are shown by "*" and "o".



(Fig. 6i, e and f), which is consistent with the PXRD pattern. New peaks belonging to the Q^4 region appear in the direct-excitation ^{29}Si MAS NMR spectrum at -109.9 and -114.0 ppm (Fig. 3a). The resonance at -117.8 ppm first detected in the $^1\text{H} \rightarrow ^{29}\text{Si}$ CP MAS NMR spectrum of the 50 h sample is now fully developed. These three peaks correspond to the three crystallographically inequivalent Si sites in the unit cell of ZSM-39.^{35,37–39} It seems that the aggregates around the organic SDA molecules formed at the beginning of the reactions have now transformed into crystalline

Fig. 6. (i) SEM images of samples obtained from the reactions quenched at 48 h (a and b), 50 h (c and d), 66 h (e and f), and 72 h (g and h). (ii) SEM images of the samples obtained from the reactions quenched at (a) 4, and (b) 14 days. (iii) SEM image of ZSM-39 crystals and two magnified images shown (100) and (111) faces. [Colour online.]



materials. The facts that the Si signals due to T_1 and T_2 sites in the MTN structure appear in the direct-excitation ^{29}Si NMR spectra later than the T_3 Si and that ^{19}F NMR signal at due to F^- occluded in $[\text{5}^{12}]$ cages (see below) only appears after 66 h heating clearly indicates that the $[\text{5}^{1264}]$ cages form first and they only join together in a later stage to form the three-dimensional MTN structure. It is apparent that the ZSM-39 crystallizes very quickly as soon as the $[\text{5}^{1264}]$ cages form in the gel.

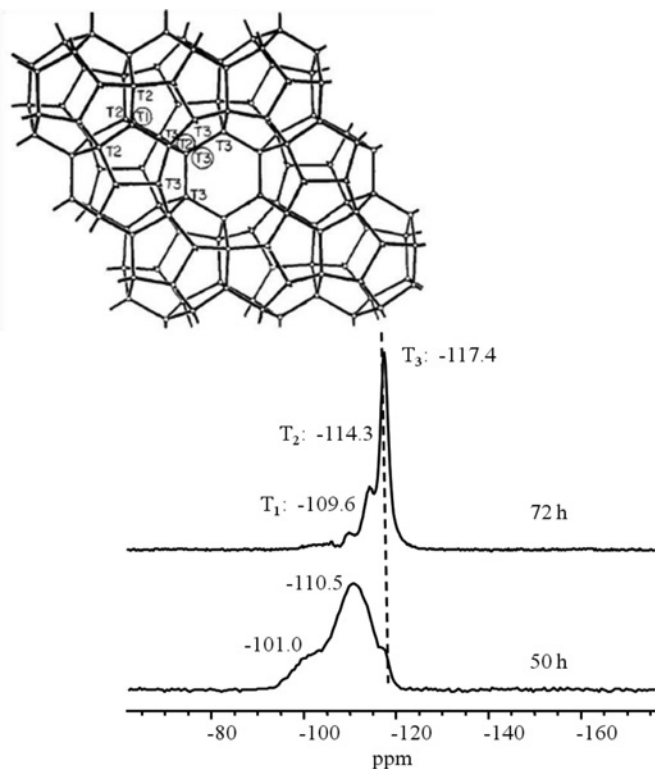
The peaks at 57.2 and 56.2 ppm in the ^{13}C CP MAS NMR spectrum (Fig. 4) are both due to the carbon from $-\text{CH}_3$ in TMA^+ . The appearance of two methyl carbon signals is due to the presence of both crystalline MTN and amorphous materials during this reaction period. In the ^{13}C CP MAS NMR spectrum of the 66 h sample (Fig. 4), the 57.2 ppm peak is assigned to the $-\text{CH}_3$ carbon atom in the TMA^+ ion that is trapped in the framework of crystalline ZSM-39, because this peak can be seen in the final product as well. The 56.2 ppm signal is due to the $-\text{CH}_3$ resonance of TMA^+ ions that are still surrounded by the amorphous gel present in the reaction mixture because the reaction is not yet completed. Formation of the three-dimensional structure traps the TMA^+ inside the cages of ZSM-39. As the distance between the $-\text{CH}_3$ carbon atoms and the oxygen atoms of MTN becomes closer, some of the electron densities from the methyl groups are drawn toward the oxygen atom, causing a downfield shift of the carbon signal of the TMA^+ . This indicates that the proximity of the methyl group to the oxygen atom is closer in the three-dimensional structure than in the amorphous gel. Furthermore, the occlusion of the TMA^+ into the final product's framework confirms that the TMA^+ ions direct the formation of ZSM-39. Finally, the peak at 46.8 ppm is due to the trimethylammonium (TMAm^+) species formed from

the decomposition of TMA^+ ions during the process of crystallization.⁴⁰ As mentioned earlier, there are two types of cages present in ZSM-39. The diameter of the smaller cavity is around 5.7 Å, whereas the larger cage is around 7.5 Å. Because the diameters of TMA^+ and TMAm^+ are around 6.9 and 6.6 Å, respectively, these two species can only reside inside the larger cavities in MTN.³⁹

Unlike the 50 h sample, for the 66 h sample, the fluoride ions have now been incorporated into the framework, which is evidenced by a new signal appearing at -81.1 ppm in the ^{19}F MAS NMR spectrum (Fig. 5). Previous work by Koller and co-workers has shown that fluoride ions occluded inside small pore zeolites displays a very wide ^{19}F chemical shift range (from -38 to -76).⁴¹ The ^{19}F chemical shift of F^- occluded in the zeolite with SGT topology is -84 ppm.⁴² Based on these literature reports, we assign the -81.1 ppm peak to the fluoride anions occluded inside ZSM-39.⁴² Furthermore, because the organic SDA species are occupying the $[\text{5}^{1264}]$ cages, the fluoride ions can only reside inside the smaller $[\text{5}^{12}]$ cages of MTN. Thus, the appearance of the -81.1 ppm peak in the ^{19}F MAS NMR spectrum of 66 h sample indicates the occlusion of the fluoride into the $[\text{5}^{12}]$ cages, therefore, by extension, it indicates the formation of crystalline ZSM-39. The simultaneous appearance of the 57.3 ppm peak and -81.1 ppm peak in the ^{13}C CP MAS and ^{19}F MAS spectra, respectively, is consistent with the formation of the MTN framework, as the positive charge due to TMA^+ in the $[\text{5}^{1264}]$ cages in the framework is balanced by the fluoride anion present in the adjacent $[\text{5}^{12}]$ cage to preserve an overall neutrality of the framework.

The reaction is near completion as it proceeds from 66 h to 72 h. At 72 h, the PXRD pattern shows sharp peaks with strong reflections that are indicative of highly crystalline ZSM-39 (Fig. 2). In the

Fig. 7. $^1\text{H} \rightarrow ^{29}\text{Si}$ CP MAS NMR spectra of the 50 h sample (contact time = 10 ms) and a 72 h sample (for comparison). The framework structure of ZSM-39 with labeled T-sites are shown.³²



^{13}C CP MAS spectrum, the signal at 56.2 ppm now disappears, and only signals at 57.2 and 46.8 ppm can be seen (Fig. 4). The diminishment of the 56.2 ppm ^{13}C signal supports that the sample is now highly crystalline, and any signals in the ^{13}C CP MAS spectrum must be due to the organic species inside the framework. In the direct-excitation ^{29}Si MAS NMR spectrum, the peaks corresponding to the three Si T-sites are very well resolved, compared with those observed at 66 h of reaction (Fig. 3a). The -123.5 ppm signal in the ^{19}F MAS NMR spectrum has decreased as a result of the formation of more crystalline materials (Fig. 5). The SEM images of the 72 h sample are shown in Figs. 6i, g and h. At higher magnification, the product crystals are often intergrown together. Furthermore, the rough surfaces of the crystals contain defects such as the edges and kinks. Some are also covered by unreacted amorphous materials.

The SEM images show that the 4 day sample is very similar to the 72 h sample and still consists of intergrown crystals (Fig. 6ii, a). After 14 days of reaction, the sample obtained is highly crystalline. The direct-excitation ^{29}Si MAS NMR spectrum shows well separated peaks for the three different Si sites (Fig. 3a). The broad peak of the Q^3 Si sites disappeared, meaning that the MTN framework formed at this point is almost perfect. The relative intensity ratio is consistent with ratio of three T-sites in the unit cell (i.e., $T_1:T_2:T_3 = 1:4:12$). Although there are still some intergrown crystals in the final product, there are many large single crystals exhibiting the dodecahedral morphology (Fig. 6ii, b).³ Further, the surfaces of the crystals obtained after 14 days of heating are much smoother, compared with those of the 4 day sample, and are mostly free from the covering of unreacted amorphous silica. These results indicate that treating the reaction mixture for a longer time helps to heal the defects in the framework and allows the production of high-quality crystals.⁴³ The peak due to the TMam^+ at 46.8 ppm in the ^{13}C CP MAS NMR spectrum is now much stronger than the signal for TMA^+ at 57.2 ppm (Fig. 4). It

seems that more TMA^+ ions have decomposed after heating for prolonged periods. The ^{19}F MAS NMR spectrum of the 14 day sample contains two peaks, the stronger one at -81.1 ppm, which corresponds to the F^- inside the smaller cages of MTN, and a weak signal at -123.5 ppm (Fig. 5). This means that there is still a very small amount of SiF_6^{2-} species present.

Throughout the course of the reaction, the other component of the eutectic mixture, 1,6-hexanediol, is not found in the solids since only the peaks due to TMA^+ and TMam^+ were observed in the ^{13}C CP MAS NMR spectra. The 1,6-hexanediol must have been dissolved and washed away by the 1:1 water and ethanol mixture during the washing process. This finding shows that 1,6-hexanediol is not occluded in ZSM-39 framework at any point of the crystallization process, indicating that the TMA^+ species is indeed the sole structure-directing component for MTN formation.

The crystals from the 14 day sample were used for AFM studies due to their large sizes (up to $70 \mu\text{m}$). All crystals exhibit a cuboctahedral shape with six square faces and eight pseudo-triangular faces (see Fig. 6iii for SEM images). Two such crystals with above-mentioned faces upward are magnified and are shown in Fig. 6iii. Both of square and pseudo-triangle faces are large and flat, where AFM could easily scan on. Also, these crystal surfaces are rarely covered by large debris or oversized nuclei, which provides good conditions for AFM scanning.

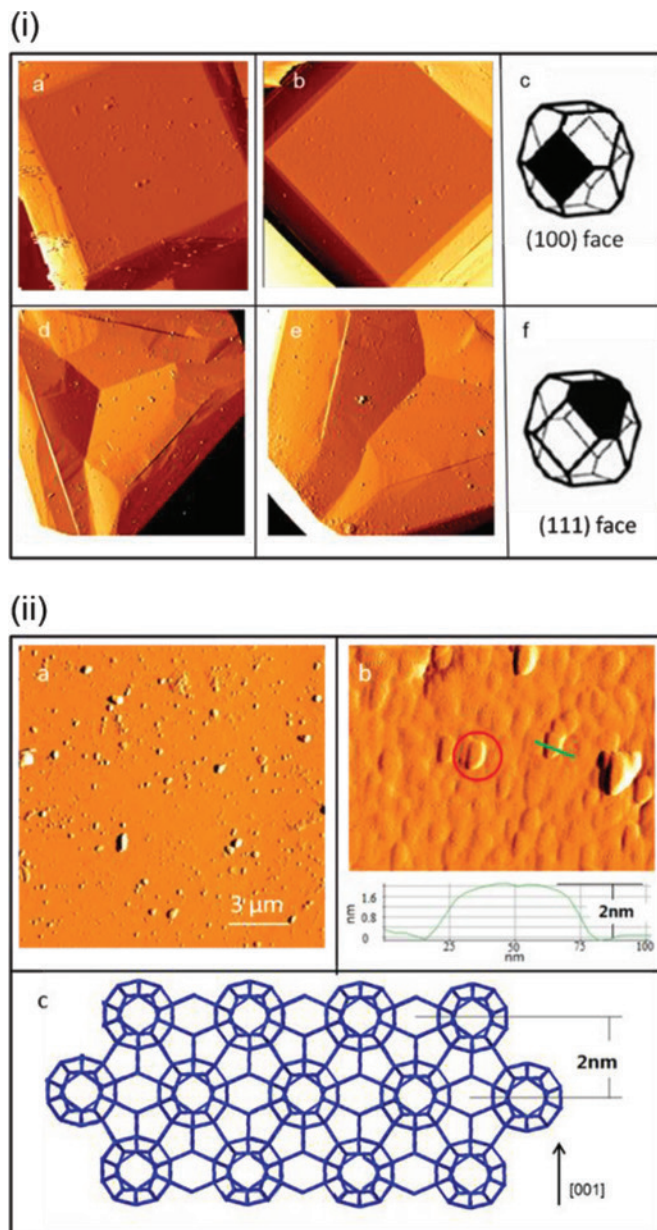
Morphology evolution mechanism of crystals belonging to cubic system was investigated in Anderson's work on zeolites with FAU topology.⁴⁴ For zeolite Y and molecular sieve SAPO-37,^{44,45} their crystal morphology is perfect octahedral, suggesting that the growth rate along $\langle 100 \rangle$ axis is much faster than that along $\langle 111 \rangle$ direction (i.e., $R = 1.73$; $R = \text{growth rate along } \langle 100 \rangle / \text{direction/growth rate along } \langle 111 \rangle \text{ direction}$).^{46,47} However, the crystal morphology of fully grown ZSM-39 crystals crystallized in a DES for 14 days is cuboctahedral (Fig. 6iii), and this morphology corresponds to $R = 1.0$,^{46,47} meaning that the growth rates along $\langle 100 \rangle$ and $\langle 111 \rangle$ directions are almost equal. It seems that both (100) and (111) planes have similar stability in the DES used.

The AFM images of ZSM-39 on (100) and (111) faces are shown in Fig. 8i, all of which are shown in the largest scan size that AFM could provide ($45 \mu\text{m} \times 45 \mu\text{m}$). Figure 8i, a is an overview AFM image of a square (100) face where the surface is flat with many nuclei on top. Figure 8i, b displays the image of a corner of the square (100) face where the angle shown is perfect 90° and the edges of the square face are very well defined. There are some minor crystal faces observed along the edges. Figure 8i, c schematically illustrates the position of the (100) face on the cubic crystal morphology.

Figures 8i, d and e show crystal (111) faces of two different crystals and Fig. 8i, f indicates the schematic position of (111) face on cuboctahedral morphology. It is worth noting that the pseudo-triangular (111) faces of both crystals are not flat. Interestingly, these (111) faces of ZSM-39 not only are non-flat, but also exhibit three-fold symmetry merging approximately at the center of the face. Each of the three contact lines (between the structures) diverging from the center of the face roughly bisects a truncated angle of the pseudo-triangular (111) face. In fact, analyses of the corresponding AFM topographic images (not shown) revealed that the observed structure is actually a tetrahedron dent with the center being approximately $1 \mu\text{m}$ deep. The cause for this intriguing structure remains unclear at this stage.

We further carried out AFM analysis of the nuclei on the (100) faces. Figure 8ii, a presents an overview AFM image of the (100) face, showing a number of large nuclei on the crystal surface with the sizes ranging from 150 and 800 nm laterally and from 30 to 150 nm in height. To capture the detailed morphological features on a smaller scale, magnified image on a very flat area in a size of $1 \mu\text{m} \times 1 \mu\text{m}$ is shown in Fig. 8ii, b. Some nuclei in this area appear to be newly born isolated nuclei and others have merged with

Fig. 8. (i) AFM error signal images (scan area: $45\ \mu\text{m} \times 45\ \mu\text{m}$) of ZSM-39: (a and b) overview images on (100) faces, (d and e) overview images on (111) faces. (ii, a) AFM error signal image on the (100) face of ZSM-39; (ii, b) magnified image on a flat area and a cross-section profile obtained from its corresponding topographic image (not shown); (ii, c) illustrative scheme of growth on along $\langle 100 \rangle$ direction. [Colour online.]



each other. The cross-section profile, which is obtained from the corresponding topographic image, is one of the newly born nuclei with sharp outline. Its size is around 2 nm in height and 50 nm in lateral dimension. Therefore, the nuclei observed from the AFM image are more like a thin terrace. Figure 8ii, c illustrates the framework structure along the $\langle 100 \rangle$ direction. As one can see, the measured height of the terrace corresponds to one layer of the unit cell. Therefore, it seems that the growth on the (100) plane is layer by layer.

Conclusions

The above results on the formation of ZSM-39 (MTN) in a solvent containing a TMACI – 1,6-hexanediol mixture indicate that the

crystallization starts with amorphous Si–O–Si units arranged around the TMA⁺ ions and then gradually forms the individual cavities similar to the [5¹²6⁴] cage in the MTN structure. As the three-dimensional framework of ZSM-39 is being established, the TMA⁺ is trapped inside the cavities of the zeolite. The [5¹²6⁴] cages are then linked together to form three-dimensional MTN structure, resulting in the formation of the [5¹²] cages where the F⁻ anions reside. The presence of TMA⁺ ions plays a key role in the formation of the [5¹²6⁴] cage. The crystallization process is also accompanied by the decomposition of TMA⁺ into TMAm⁺ species. 1,6-Hexanediol has no structure-directing role. A longer reaction time at a higher temperature yields single crystals with low defects. Surface analyses by AFM and SEM suggest that the growth rates along $\langle 100 \rangle$ and $\langle 111 \rangle$ faces appear to be similar and that the growth on (100) surface proceeds in a layer by layer fashion (where a layer means a layer of unit cell).

Our investigation provides an example of a mechanistic study on completely siliceous zeolite formation in a solvent involving an eutectic mixture. Utilization of an array of techniques including PXRD, NMR, SEM, and AFM allows us to gain new physical insights into a number of issues regarding the formation of zeolite ZSM-39 such as the role of each component of the eutectic mixture in crystallization, identifying key structural units in precursors leading to MTN structure, and information on the growth rates along different crystallographic directions. As mentioned earlier, water can affect ionothermal synthesis of zeolites, but the exact role of water in the current system is still not clear and further studies are needed.

Acknowledgements

Y.H. thanks the Natural Sciences and Engineering Research Council of Canada for a Discovery grant and a Discovery Accelerator grant. Funding from Canada Research Chair program is also acknowledged.

References

- (1) Cambor, M. A.; Hong, S. B. In *Porous Materials*; Bruce, D. W., O'Hare, D., Walton, R. I., Eds.; John Wiley & Sons: Chichester, United Kingdom, 2010; pp. 265–325.
- (2) *Introduction to Zeolite Science and Practice*. van Bekkum, H., Flanigen, E. M., Jacobs, P. A., Jansen, J. C., Eds.; Elsevier Science, Amsterdam, Netherlands, 2001.
- (3) Schlenker, J. L.; Dwyer, F. G.; Jenkins, E. E.; Rohrbaugh, W. J.; Kokotailo, G. T.; Meier, W. M. *Nature* **1981**, 294, 340. doi:10.1038/294340a0.
- (4) Bibby, D. M.; Parker, L. M. *Zeolites* **1983**, 3, 11. doi:10.1016/0144-2449(83)90079-9.
- (5) Long, Y.; He, H.; Zheng, P.; Wu, G.; Wang, B. *J. Incl. Phenom.* **1987**, 5, 355. doi:10.1007/BF00665368.
- (6) Marler, B.; Dehnhostel, N.; Eulert, H. H.; Gies, H.; Liebau, F. *J. Incl. Phenom.* **1986**, 4, 339. doi:10.1007/BF00665616.
- (7) Ripmeester, J. A.; Desando, M. A.; Handa, Y. P.; Tse, J. S. *J. Chem. Soc., Chem. Commun.* **1988**, 608. doi:10.1039/C39880000608.
- (8) Anthony, J. L.; Davis, M. E. In *Self-Organized Nanoscale Materials*; Lockwood, D. J., Ed.; Springer, New York, 2006; pp. 159–185.
- (9) Seral, J. J.; Uriel, S.; Coronas, J. *Eur. J. Inorg. Chem.* **2008**, 2008, 4915. doi:10.1002/ejic.200800682.
- (10) Tang, X.; Sun, Y.; Wu, T.; Wang, L.; Fei, L.; Long, Y. *J. Chem. Soc. Faraday Trans.* **1993**, 89, 1839. doi:10.1039/ft9938901839.
- (11) Bibby, D. M.; Baxter, N. I.; Grant-Taylor, D.; Parker, L. M. In *Zeolite Synthesis*; American Chemical Society, 1989, Vol. 398, pp. 209–220.
- (12) Caulet, P.; Hazm, J.; Guth, J. L.; Joly, J. F.; Lynch, J.; Raatz, F. *Zeolites* **1992**, 12, 240. doi:10.1016/S0144-2449(05)80290-8.
- (13) Kanno, N.; Miyake, M.; Sato, M. *Zeolites* **1994**, 14, 625. doi:10.1016/0144-2449(94)90118-X.
- (14) Uguina, M. A.; de Lucas, A.; Ruiz, F.; Serrano, D. P. *Ind. Eng. Chem. Res.* **1995**, 34, 451. doi:10.1021/ie00041a004.
- (15) Xu, W.; Li, J.; Liu, G. *Zeolites* **1990**, 10, 753. doi:10.1016/0144-2449(90)90057-X.
- (16) Xu, W.; Li, J.; Li, W.; Zhang, H.; Liang, B. *Zeolites* **1989**, 9, 468. doi:10.1016/0144-2449(89)90040-7.
- (17) Xu, H.; Kong, Y.; L., L.; Li, J. P.; Wang, J. G.; Dong, J. *Acta Petrol. Sin.* **2006**, 22, 153.
- (18) Shi, Q.; Yu, J.; Liu, L.; Li, J. P.; Dong, J. *Acta Petrol. Sin.* **2008**, 24, 185.
- (19) Liu, L.; Li, X.; Xu, H.; Li, J.; Lin, Z.; Dong, J. *Dalton Trans.* **2009**, 10418. doi:10.1039/B912785B.
- (20) Cai, R.; Liu, Y.; Gu, S.; Yan, Y. *J. Am. Chem. Soc.* **2010**, 132, 12776. doi:10.1021/ja101649b.

- (21) Lin, Z. S.; Huang, Y. *Microporous Mesoporous Mater.* **2016**, *224*, 75. doi:10.1016/j.micromeso.2015.11.008.
- (22) Lin, Z. S.; Huang, Y. *Can. J. Chem.* **2016**, *94* (6), 533. doi:10.1139/cjc-2016-0115.
- (23) Sachse, A.; Wuttke, C.; Lissner, E.; Oberson de Souza, M. *Chem. Eur. J.* **2014**, *20*, 14996. doi:10.1002/chem.201404568.
- (24) Wen, H.; Zhou, Y.; Xie, J.; Long, Z.; Zhang, W.; Wang, J. *RSC Adv.* **2014**, *4*, 49647. doi:10.1039/C4RA07627C.
- (25) Wheatley, P. S.; Allan, P. K.; Teat, S. J.; Ashbrook, S. E.; Morris, R. E. *Chem. Sci.* **2010**, *1*, 483. doi:10.1039/c0sc00178c.
- (26) Yuan, D.; He, D.; Xu, S.; Song, Z.; Zhang, M.; Wei, Y.; He, Y.; Xu, S.; Liu, Z.; Xu, Y. *Microporous Mesoporous Mater.* **2015**, *204*, 1. doi:10.1016/j.micromeso.2014.10.049.
- (27) Ma, Y. C.; Wang, S. J.; Song, Y. L.; Xu, Y. P.; Tian, Z. J.; Yu, J. Y.; Lin, L. W. *Chin. J. Inorg. Chem.* **2010**, *26*, 1923.
- (28) Tendeloo, L. van; Haouas, M.; Martens, J. A.; Kirschhock, C. E. A.; Breynaert, E.; Taulelle, F. *Faraday Discuss.* **2015**, *179*, 437. doi:10.1039/C4FD00234B.
- (29) de Moor, P. P. E. A.; Beelen, T. P. M.; Komanshek, B. U.; Beck, L. W.; Wagner, P.; Davis, M. E.; van Santen, R. A. *Chem. Eur. J.* **1999**, *5*, 2083. doi:10.1002/(SICI)1521-3765(19990702)5:7<2083::AID-CHEM2083>3.0.CO;2-F.
- (30) Parnham, E. R.; Morris, R. E. *Acc. Chem. Res.* **2007**, *40*, 1005. doi:10.1021/ar700025k.
- (31) Yasaka, Y.; Wakai, C.; Matubayasi, N.; Nakahara, M. *J. Phys. Chem. A* **2007**, *111*, 541. doi:10.1021/jp0673720.
- (32) Ma, H.; Tain, Z.; Xu, R.; Wang, B.; Wei, Y.; Wang, L.; Xu, Y.; Zhang, W.; Lin, L. *J. Am. Chem. Soc.* **2008**, *130*, 8120. doi:10.1021/ja802207p.
- (33) Nagy, J. B.; Derouane, E. G. In *Perspectives in Molecular Sieve Science*; American Chemical Society, 1988, Vol. 368, pp. 2–32.
- (34) Zhang, G.; Wang, B.; Zhang, W.; Li, M.; Tian, Z. *Dalton, Trans.* **2016**, *45*, 6634. doi:10.1039/C6DT00424E.
- (35) Fyfe, C. A.; Gies, H.; Feng, Y. *J. Am. Chem. Soc.* **1989**, *111*, 7702. doi:10.1021/ja00202a006.
- (36) Gies, H. Z. *Kristallogr.* **1984**, *167*, 73. doi:10.1524/zkri.1984.167.1-2.73.
- (37) Fyfe, C. A.; Gies, H.; Feng, Y. *J. Chem. Soc., Chem. Commun.* **1989**, 1240. doi:10.1039/C39890001240.
- (38) Fyfe, C. A.; Gies, H.; Feng, Y.; Kokotailo, G. T. *Nature* **1989**, *341*, 223. doi:10.1038/341223a0.
- (39) Higgins, J. B.; Woessner, D. E.; Trewella, J. C.; Schlenker, J. L. *Zeolites* **1984**, *4*, 112. doi:10.1016/0144-2449(84)90047-2.
- (40) Dewaele, N.; Gabelica, Z.; Bodart, P.; Nagy, J. B.; Giordano, G.; Derouane, E. G. In *Studies in Surface Science and Catalysis*; Grobet, P. J., Mortier, W. J., Vansant, E. F., Schulz-Ekloff, G., Eds.; Elsevier, 1988, Vol. 37, pp. 65–73.
- (41) Camblora, M. A.; Barretta, P. A.; Diaz-Cabañas, M. J.; Villaescusa, L. A.; Pucheá, M.; Boixa, T.; Pérez, E.; Koller, H. *Microporous Mesoporous Mater.* **2001**, *48*, 11. doi:10.1016/S1387-1811(01)00325-0.
- (42) Zones, S. I.; Darton, R. J.; Morris, R.; Hwang, S.-J. *J. Phys. Chem. B* **2005**, *109*, 652. doi:10.1021/jp0402434.
- (43) Subotić, B.; Bronić, J. In *Handbook of Zeolite Science and Technology*; Auerbach, S. M., Carrado, K. A., Dutta, P. K., Eds.; Marcel Dekker, Inc., New York, 2003.
- (44) Anderson, M. W.; Agger, J. R.; Thornton, J. T.; Forsyth, N. *Angew. Chem. Int. Ed.* **1996**, *35*, 1210. doi:10.1002/anie.199612101.
- (45) Zhang, L.; Chen, D.; Nie, H.-Y.; Huang, Y. *Microporous Mesoporous Mater.* **2013**, *175*, 147. doi:10.1016/j.micromeso.2013.03.026.
- (46) Choi, K.-S. *Dalton Trans.* **2008**, 5432. doi:10.1039/B807848C.
- (47) Wang, Z. L. *J. Phys. Chem. B* **2000**, *104*, 1153. doi:10.1021/jp993593c.